Acta Crystallographica Section F
Structural Biology Communications
ISSN 2053-230X

A structural characterization of the isoniazid *Mycobacterium tuberculosis* drug target, Rv2971, in its unliganded form

Adam Shahine,[a] Anggia Prasetyoputri,[a,b] Jamie Rossjohn[a,c] and Travis Beddoe[a,d]*

[a]Department of Biochemistry and Molecular Biology, Monash University, Clayton, Victoria, Australia, [b]Research Centre for Biotechnology, Indonesian Institute of Sciences (LIPI), Indonesia, [c]Institute of Infection and Immunity, School of Medicine, Cardiff University, Heath Park, Cardiff CF14 4XN, Wales, and [d]Department of Agriculture Sciences, La Trobe University, Bundoora, Victoria, Australia

Correspondence e-mail: travis.beddoe@monash.edu

Received 25 February 2014
Accepted 31 March 2014

PDB reference: Rv2971, 4otk

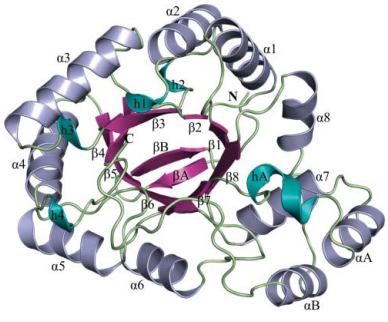

Aldo-keto reductases (AKR) are a large superfamily of NADPH-dependent oxidoreductases and play a role in detoxification of toxic metabolites. Rv2971, an AKR in *Mycobacterium tuberculosis*, has recently been identified as a target of isoniazid, a key first-line drug against tuberculosis. Here, the cloning, expression, purification, crystallization and structural characterization of Rv2971 are described. To gain insight into its function, the crystal structure of Rv2971 was successfully determined to 1.60 Å resolution in its unliganded form. The structure exhibits a TIM-barrel fold typical of AKRs, revealing structural characteristics essential for function and substrate specificities, allowing a structural comparison between Rv2971 and other mycobacterial AKRs.

1. Introduction

Mycobacterium tuberculosis, the aetiological agent of tuberculosis (TB), remains a major health burden globally, resulting in approximately 1.4 million deaths annually (World Health Organization, 2013). The emergence of drug-resistant strains underlines the urgent need for the development of new anti-mycobacterial therapeutics. Multiple drug resistant strains of TB (MDR-TB), and more recently extensively drug-resistant strains of TB (XDR-TB), are classified as expressing resistance to at least two of the first-line anti-TB drugs and a number of second-line anti-TB drugs, resulting in a limited means of treating diseased patients.

The key first-line drug in TB treatment is isoniazid (INH), a hydrazide prodrug activated by the catalase-peroxidase KatG to produce INH–NAD(P) adducts that exhibit potent anti-mycobacterial activity (Rozwarski *et al.*, 1998; Timmins & Deretic, 2006). The primary target of the INH–NAD(P) adduct is InhA, an enoyl-acyl carrier protein reductase that plays an essential role in mycolic acid biosynthesis (Dessen *et al.*, 1995). In addition to InhA, the drug acts against 17 recently identified targets within *M. tuberculosis* (Argyrou *et al.*, 2006). These targets exhibit a variety of essential roles implemented in the fitness and survival of the mycobacterium, and provide a variety of potential candidates for the development of new anti-TB therapeutics.

One of the targets identified is the essential aldo-keto reductase (AKR) AKR5H1 encoded by the gene *rv2971*. *rv2971* has previously been characterized as an essential gene for growth and survival in *M. tuberculosis* (Sassetti *et al.*, 2003) with a potential role in the detoxification of toxic metabolites (Grimshaw, 1992; Grant *et al.*, 2003; Penning & Drury, 2007). Recently, the catalytic activity of Rv2971 and its *M. smegmatis* orthologue MSMEG_2407 (67% sequence identity) has been characterized, revealing differences in dicarbonyl substrate specificities and affinities (Scoble *et al.*, 2010). The potency of INH was characterized against both enzymes, revealing a higher affinity against MSMEG_2407 compared with Rv2971, with apparent K_i values of 6.0 ± 1.2 and 31.0 ± 1.4 μ*M* reported, respectively (Scoble *et al.*, 2010).

To gain functional insight into the role of AKR5H1, the crystal structure of MSMEG_2407 has been determined in its apo form and in its holoenzyme form in the presence of NADPH (Scoble *et al.*, 2010). The crystal structure reveals an $(\alpha/\beta)_8$-barrel topology, or a TIM-barrel fold, typical of other AKRs as previously described

Table 1
Data-collection and refinement statistics for Rv2971.

Values in parentheses are indicative of the highest resolution shell.

Data collection	
Diffraction source	MX2, Australian Synchrotron
Detector	ADSC Quantum 315r CCD
Space group	$P3_22_1$
Unit-cell parameters (Å, °)	$a = b = 86.27$, $c = 86.29$, $\alpha = 90.0$ $\beta = 90.0$ $\gamma = 120.0$
Wavelength (Å)	0.95370
Resolution range (Å)	38.58–1.60 (1.66–1.60)
Total No. of reflections	525473 (76789)
No. of unique reflections	49373 (4857)
Completeness (%)	100.0 (100.0)
Mean $I/\sigma(I)$†	12.72 (2.35)
R_{merge}‡ (%)	11.4 (91.7)
$R_{p.i.m.}$‡ (%)	3.7 (29.1)
Multiplicity	10.6 (10.8)
Structural refinement	
Resolution range (Å)	38.59–1.60 (1.63–1.60)
R_{work}§ (%)	13.60 (22.67)
R_{free}§ (%)	16.90 (27.59)
R.m.s.d.,¶ bond lengths (Å)	0.006
R.m.s.d.,¶ bond angles (°)	1.05
Ramachandran plot	
Favoured (%)	98.20
Allowed (%)	1.80
Outliers (%)	0.00
No. of modelled non-H atoms	
Macromolecules	2128
Ligands	15
Water	311
Protein residues	276
Wilson B factor (Å^2)	18.51
Average B factors (Å^2)	
Protein atoms	20.40
Ligand molecules	20.40
Water molecules	33.70
PDB code	4otk

† I is the integrated intensity and $\sigma(I)$ is the estimated standard deviation of that intensity. ‡ $R_{merge} = \sum_{hkl}\sum_i |I_i(hkl) - \langle I(hkl)\rangle| / \sum_{hkl}\sum_i I_i(hkl)$ where $I_i(hkl)$ is the scaled intensity of the ith measurement and $\langle I(hkl)\rangle$ is the mean intensity for that reflection. $R_{p.i.m.} = R_{merge}$ divided by the multiplicity. § $R_{work} = \sum_{hkl} ||F_{obs}| - |F_{calc}|| / \sum_{hkl} |F_{obs}|$ for all data excluding the 5% that comprise the R_{free} used for cross-validation. ¶ Root-mean-square deviation from ideal values (Engh & Huber, 1991).

(Banner *et al.*, 1975), and enabled residues essential for enzyme kinetic activity and cofactor binding to be ascertained. While the crystal structure of MSMEG_2407 provides invaluable information on its functionality, Rv2971 possesses a number of differences in these binding pockets.

Here, we determined the crystal structure of Rv2971 in its unliganded form to a resolution of 1.60 Å. The structure enables the characterization of the substrate and NADPH binding pockets, revealing the subtle architectural differences between Rv2971 and MSMEG_2407, and providing insight into the differences in substrate specificities and INH inhibition levels. In addition, the Rv2971 structure may provide an initial template for the development of new anti-mycobacterial therapeutics.

2. Materials and methods

2.1. Cloning, expression and purification of recombinant protein

The gene encoding Rv2971 was cloned, overexpressed and purified as soluble recombinant protein as previously described (Scoble *et al.*, 2010). For crystallization experiments, the purified recombinant protein was buffer-exchanged into 10 m*M* Tris–HCl pH 8.0, 200 m*M* NaCl and concentrated to 7 mg ml^{-1}. The concentration of purified Rv2971 was determined spectrophotometrically (NanoDrop 1000, Thermo Scientific) at 280 nm and was calculated using an extinction coefficient of 28 545 M^{-1} cm^{-1}. The molecular weight, purity and identity of the protein were confirmed by SDS–PAGE and Western blotting with anti-hexahistidine antibody (R&D Systems).

2.2. Crystallization

The initial crystallization experiments involved screening 192 conditions from commercially available kits from Hampton Research (Crystal Screen HT and PEG/Ion HT) using a CrystalMation (Rigaku) integrated robotic workstation and the sitting-drop vapour-diffusion technique. Rod-shaped crystals were obtained initially at a

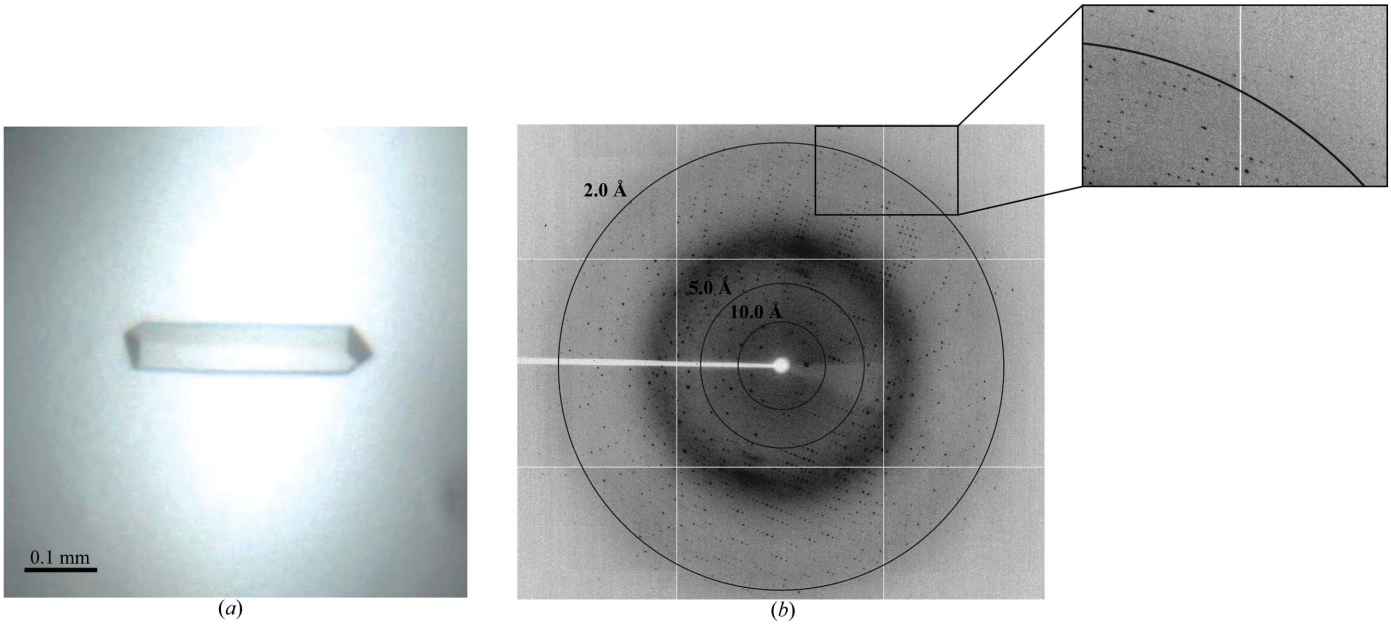

(*a*) (*b*)

Figure 1
Crystallization and data collection of Rv2971. (*a*) Crystal of Rv2971 obtained from 7 mg ml^{-1} protein solution (in 10 m*M* Tris–HCl pH 8.0, 200 m*M* NaCl) using 0.2 *M* sodium malonate pH 5.0, 19%(*w*/*v*) PEG 3350. (*b*) A typical 0.50° oscillation image from an Rv2971 crystal flash-cooled in 15%(*v*/*v*) glycerol.

protein concentration of 7 mg ml^{-1} at 277 K after 24 h of equilibration against a crystallization condition comprised of 0.2 *M* sodium malonate pH 5.0, 20%(*w*/*v*) polyethylene glycol (PEG) 3350. Larger crystals of high diffraction quality were obtained by optimizing the crystal condition in 24-well Linbro plates (Hampton Research). The crystallization condition was optimized by fine-tuning the pH, protein concentration and precipitant concentration using a hanging drop consisting of 1 µl protein solution and 1 µl precipitant solution and a 500 µl reservoir volume (Fig. 1*a*). The best crystals appeared after 24 h of equilibration against a crystallization condition comprised of 0.2 *M* sodium malonate pH 5.0, 19%(*w*/*v*) PEG 3350 at a protein concentration of 7 mg ml^{-1} and grew to full size in 2 d.

2.3. X-ray data collection

For X-ray diffraction data collection, crystals of Rv2971 were transferred to a CryoLoop and soaked in a cryoprotectant consisting of 19%(*v*/*v*) PEG 3350, 0.2 *M* sodium malonate pH 5.0, 15%(*w*/*v*) glycerol before cooling to 100 K in a nitrogen-gas stream. A complete data set was collected from a single crystal on the MX2 beamline at the Australian Synchrotron using an ADSC Quantum 315rr CCD detector. A total of 360 frames of 0.5° were recorded with an exposure time of 1 s per frame (Fig. 1*b*). The data were processed using *iMosflm* (Battye *et al.*, 2011) and various programs from the *CCP*4 suite such as *SCALA* and *POINTLESS* (Winn *et al.*, 2011). The final statistics of data collection and processing are summarized in Table 1.

2.4. Structural determination

The crystal structure of Rv2971 was determined by the molecular-replacement method with *Phaser-MR* as part of the *PHENIX* program suite (Adams *et al.*, 2010). The coordinates of *M. smegmatis* AKR5H1 MSMEG_2407 (67% sequence identity; PDB entry 2wzm; Scoble *et al.*, 2010) were used as the search model. The resultant LLG score and TZF score obtained were 2010.15 and 43.8, respectively. For cross-validation, a random set of 5% of the total reflections were kept aside from the refinement and used for the calculation of $R_{\rm free}$ (Brünger, 1992). The initial model was refined as a rigid body followed by TLS refinement using TLS groups as suggested by the *TLSMD* server (Painter & Merritt, 2006). The TLS refinement was performed according to four TLS groups, which are A8–A171, A172–A188, A189–A257 and A258–A283. The model obtained was manually adjusted using the interactive graphics program *Coot* (Emsley *et al.*, 2010) and refined using *phenix.refine* (Adams *et al.*, 2010) until no further improvement of the model could be made. Atomic coordinates and structure factors have been deposited in the Protein Data Bank under accession code 4otk. The final statistics of structural refinement are summarized in Table 1.

2.5. Structural analysis

Refinement validation was conducted using *MolProbity* and the *POLYGON* tools in the *PHENIX* program suite (Adams *et al.*, 2010; Chen *et al.*, 2010). Secondary structure was confirmed by the *STRIDE* plugin in *PyMOL* (Zhu, 2011). All structural superpositions were achieved using the SSM superpose feature of *Coot* (Emsley *et al.*, 2010). Electrostatic surface distribution calculations were performed using the *APBS* plugin for *PyMOL* (Baker *et al.*, 2001). The *M. smegmatis* AKRH5 MSMEG_2407 holoenzyme crystal structure (PDB entry 2wzm) and the apo crystal structure (PDB entry 2wzt; Scoble *et al.*, 2010) were used for structural alignments.

3. Results and discussion

3.1. Structural determination of Rv2971

To gain structural insight into the isoniazid drug target Rv2971, the crystal structure of the *M. tuberculosis* protein was determined. Recombinant *M. tuberculosis* Rv2971 was expressed, purified and crystallized using vapour-diffusion methods (Fig. 1*a*). Rv2971 was purified as a monomer as determined by size-exclusion chromatography, and routinely produced yields of 2 mg of pure protein per litre. Crystals belonged to the trigonal space group $P3_221$, with unit-cell parameters $a = b = c = 86.3$ Å, $\alpha = \beta = 90.0°$, $\gamma = 120.0°$. A complete data set was collected to a resolution of 1.60 Å from a single crystal at 100 K (Fig. 1*b*), with data collection and processing summarized in Table 1. Based on Matthews coefficient calculations, one polypeptide chain (59.96% solvent content) could be accom-

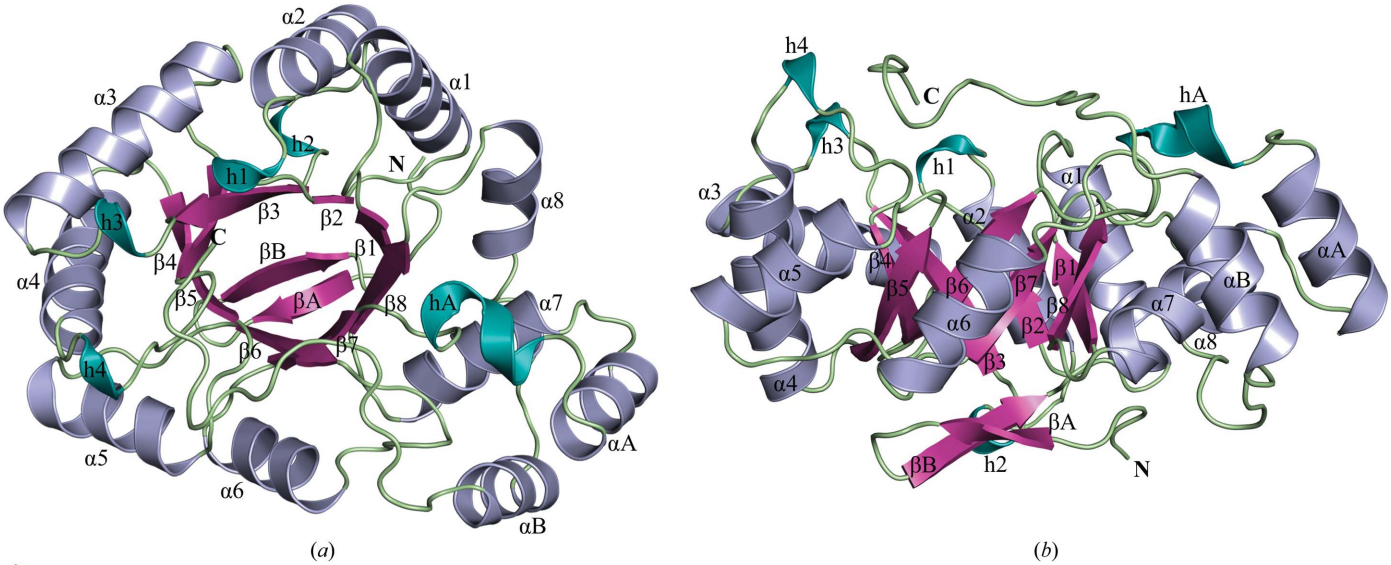

Figure 2
Overall crystal structure of Rv2971. Cartoon representation of the (*a*) top view and (*b*) side view rotated 90° of the overall structure. The C- and N-termini of the structure are labelled, with secondary-structure elements β-strands, α-helices and 3_{10}-helices, as calculated by *STRIDE* (Zhu, 2011), coloured magenta, blue and cyan, respectively. All figures were prepared in *PyMOL*.

modated in the asymmetric unit, with a calculated V_M value of 3.07 Å^3 Da^{-1} (Matthews, 1968).

The crystal structure of Rv2971 was determined to 1.60 Å resolution *via* molecular replacement using the *M. smegmatis* orthologue, MSMEG_2407, as a search model (PDB entry 2wzm), with final R_{work} and R_{free} statistics of 13.90 and 16.90%, respectively. Refinement statistics are summarized in Table 1. Of the construct utilized in crystallization, the large vector-derived N-terminal domain (MGSSH6SSGLVPRGSHMASMTGGQQMGRGSEF) was unstructured and residues 7–282 of Rv2971 were modelled into the electron density. The final model consisted of 276 amino-acid residues and 311 water molecules. The final model also included two malonate ions and two chloride ions originating from the crystallization condition and crystallization buffer, respectively. A Ramachandran plot analysis of the final model by C^{α} geometry validation (Lovell *et al.*, 2003) showed that 98.2% of the residues are in the most favoured regions, while 1.8% of residues are within the allowed regions.

3.2. Overall crystal structure of Rv2971

The overall 1.60 Å resolution crystal structure of Rv2971 in its unliganded form (Figs. 2*a* and 2*b*) adopts an $(\alpha/\beta)_8$-barrel topology, or a TIM-barrel fold, as previously described (Banner *et al.*, 1975). The structural fold exhibits typical characteristics of AKR substrates,

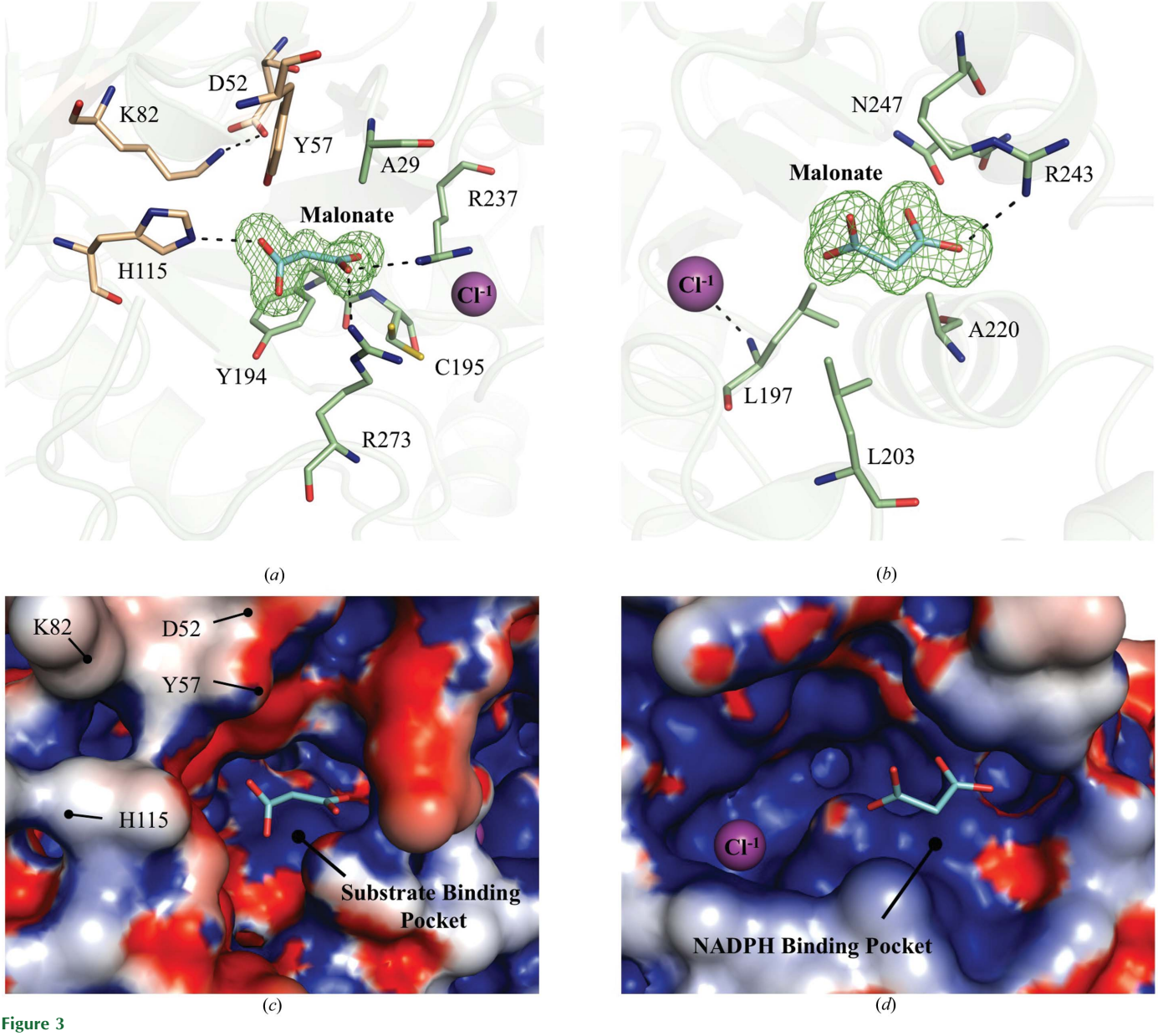

Figure 3
Rv2971 substrate and cofactor binding pocket architecture. Cartoon representation of (*a*) the substrate binding pocket and (*b*) the NADPH binding pocket. Two malonate ions and a single chloride ion bound during crystallization are represented as cyan sticks and magenta spheres, respectively. Electron density of maps is shown as $F_o - F_c$ simulated-annealing OMIT maps contoured at 3σ. Amino-acid residues involved in binding to the malonate and chloride ions are represented as green sticks. Hydrogen-bond formation between contact residues and ions is represented as black dashes, with bond distances ranging between 2.6 and 3.6 Å. The Asp52-Tyr57-Lys82-His115 catalytic tetrad is represented in wheat. The solvent-accessible surface representation coloured by electrostatic potential of the (*c*) substrate binding pocket and (*d*) NADPH binding pocket was calculated by *APBS* (Baker *et al.*, 2001). The potential contours are shown on a scale from +5.0 (blue) to −5.0 k_BT e^{-1} (red); white indicates a value close to 0 k_BT e^{-1}. Indicated are the positions of the Asp52-Tyr57-Lys82-His115 catalytic tetrad.

where the TIM barrel is comprised of eight β-strands (β1–β8), flanked by eight α-helices (α1–α8) interwoven in an antiparallel manner between each β-strand. Situated at the N-terminus of the structure are two antiparallel β-stands (βA and βB) that cover the base of the protein structure (Fig. 2*b*). The TIM-barrel structure is punctuated by two α-helices (αA and αB) on the C-terminal side of the protein structure (Fig. 2*a*). Dispersed through the C-terminal side, or 'open rim' face, of the protein structure are a series of 3_{10}-helices (h1, h3, h4 and hA) that contribute to the overall α-helical content of the Rv2971 structure by forming the NADPH binding pocket.

3.3. Substrate and NADPH binding pockets of Rv2971

The crystal structure of Rv2971 was determined in the presence of two malonate ions bound within the substrate binding pocket and NADPH binding pocket. Attempts to soak NADPH into the crystals were unsuccessful because of the presence of the malonate ions blocking the binding pockets. Within the substrate binding pocket, the malonate ion is bound to Rv2971 *via* hydrogen bonding with Asp52 and His115 at a bond distance of 2.6 and 2.9 Å, respectively (Fig. 3*a*). Residues Asp52 and His115 belong to the Asp-Tyr-Lys-His catalytic tetrad typical of AKRs. In the case of Rv2971, the catalytic tetrad is comprised of residues Asp52-Tyr57-Lys82-His115. A single chloride ion is bound between the substrate and NADPH binding pockets, and is bound to residue Leu197 *via* hydrogen bonding (Fig. 3*b*). A second malonate ion is bound within the NADPH pocket, binding residues involved in contacts with NADPH *via* hydrogen-bond formation, with bond distances ranging between 3.0 and 3.6 Å (Fig. 3*b*). Both the substrate and NADPH binding pockets are electrostatically positively charged (Figs. 3*c* and 3*d*) which, as well as being highly surface exposed, facilitates the substrate and NADPH binding capabilities of Rv2971.

3.4. Structural comparison with the *M. smegmatis* orthologue MSMEG_2407

With the successful determination of the crystal structure of Rv2971, a structural comparison was conducted with MSMEG_2407 to characterize the previously observed differences in enzyme kinetic activity (Scoble *et al.*, 2010). The crystal structures of Rv2971 and the

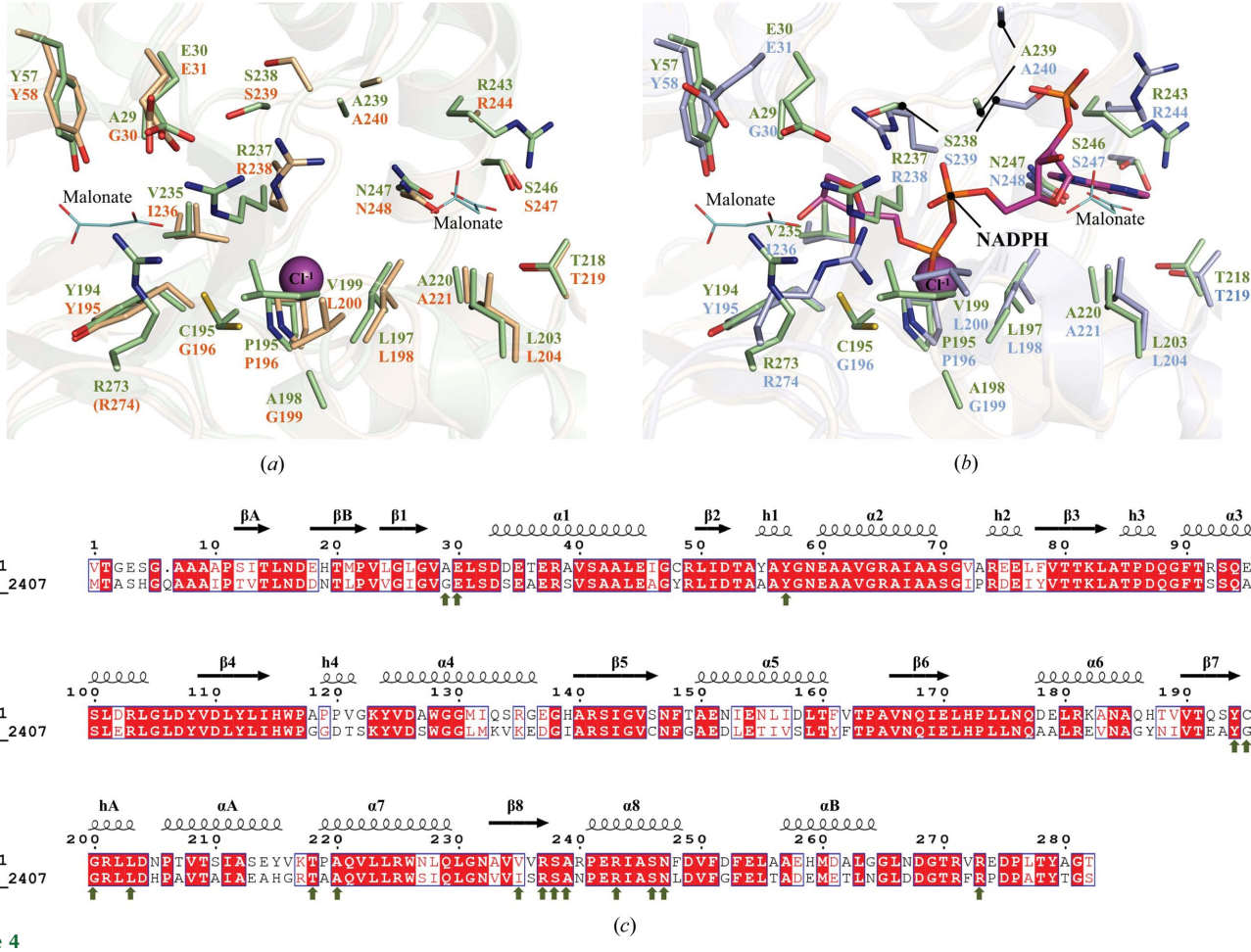

Figure 4
Structural comparison between Rv2971 and MSMEG_2407. Ball-and-stick representation of the NADPH binding pockets of Rv2971 and (*a*) MSMEG_2407 in its apo form (PDB entry 2wzt) and (*b*) in its holoenzyme form in the presence of NADPH (PDB entry 2wzm). Visualized is the structural comparison between amino-acid residues in contact with NADPH in the MSMEG_2407 holoenzyme structure with residues of identical position in Rv2971. Residues of Rv2971, the MSMEG_2407 apo form and the MSMEG_2407 holoenzyme are represented in green, wheat and blue, respectively. Bound malonate ions and a single chloride ion are represented as cyan lines and magenta spheres, respectively. The bound NADPH molecule in the MSMEG_2407 holoenzyme is represented in pink. Missing residues are indicated in parentheses. (*c*) Sequence alignment between Rv2971 and MSMEG_2407. The alignment was prepared with the program *ClustalW*2 and visualized using *ESPript* v.2.2. The secondary-structure elements correspond to the structure of Rv2971. Strict sequence-identical residues are denoted with a red background, while similar residues are visualized in red text with white background. Sequence similarities in groups are denoted by blue boxes. MSMEG_2407 residues interacting with NADPH by hydrogen bonding or van der Waals interactions are indicated by green arrows.

apo form of MSMEG_2407 overlaid tightly, with an overall r.m.s.d. value of 0.85 Å observed. While Rv2971 and MSMEG_2407 share a sequence identity of 67%, a number of substitutions are present between amino-acid residues within the NADPH binding pocket that impact on the enzyme kinetic activity rates between the orthologues (Fig. 4). Of the 21 amino-acid residues from MSMEG_2407 interacting with NADPH, there is a difference of four residues in Rv2971. Residues Gly30, Gly196, Leu200 and Ile236 in MSMEG_2407 are substituted with residues Ala29, Cys195, Val199 and Val235 (Fig. 4). The most significant difference is the substitution of a glycine (Gly196) for cysteine (Cys195). Cys195 is present in two alternate conformations in the structure of Rv2971, both facing into the NADPH binding pocket. One of the conformations forms van der Waals interactions with the chloride ion present (Fig. 4*a*), and indicates the potential position of the residue in the presence of NADPH, owing to the position of a hydroxyl group of NADPH bound in MSMEG_2407 (Fig. 4*b*). The loss of glycine residues involved in NADPH contacts indicates a more constrained binding site, in particular the substitution of Gly30 for Ala29 at the nicotinamide binding site, and may provide a more complete holoenzyme crystal structure of AKR5H1, which appeared disordered in the MSMEG_2407 holoenzyme crystal structure (Scoble *et al.*, 2010).

4. Concluding remarks

While valuable structural insight into the architecture of Rv2971 has been obtained, the successful determination of further crystal structures of Rv2971, both in its holoenzyme form and in complex with the INH–NADP adduct, will aid in further characterization of its function, as well as in gaining a more in-depth characterization of INH resistance.

We thank the staff of the Australian Synchrotron and Monash Macromolecular Crystallization Facility for assistance with crystallization and X-ray data collection. This work was supported by the Australian Research Council (ARC) Centre of Excellence in Structural and Functional Microbial Genomics and the National Health and Medical Research Council of Australia. JR is an NHMRC Australia Fellow and TB is a Pfizer Australian Research Fellow.

References

Adams, P. D. *et al.* (2010). *Acta Cryst.* D**66**, 213–221.
Argyrou, A., Jin, L., Siconilfi-Baez, L., Angeletti, R. H. & Blanchard, J. S. (2006). *Biochemistry*, **45**, 13947–13953.
Baker, N. A., Sept, D., Joseph, S., Holst, M. J. & McCammon, J. A. (2001). *Proc. Natl Acad. Sci. USA*, **98**, 10037–10041.
Banner, D. W., Bloomer, A. C., Petsko, G. A., Phillips, D. C., Pogson, C. I., Wilson, I. A., Corran, P. H., Furth, A. J., Milman, J. D., Offord, R. E., Priddle, J. D. & Waley, S. G. (1975). *Nature (London)*, **255**, 609–614.
Battye, T. G. G., Kontogiannis, L., Johnson, O., Powell, H. R. & Leslie, A. G. W. (2011). *Acta Cryst.* D**67**, 271–281.
Brünger, A. T. (1992). *Nature (London)*, **355**, 472–475.
Chen, V. B., Arendall, W. B., Headd, J. J., Keedy, D. A., Immormino, R. M., Kapral, G. J., Murray, L. W., Richardson, J. S. & Richardson, D. C. (2010). *Acta Cryst.* D**66**, 12–21.
Dessen, A., Quémard, A., Blanchard, J. S., Jacobs, W. R. Jr & Sacchettini, J. C. (1995). *Science*, **267**, 1638–1641.
Emsley, P., Lohkamp, B., Scott, W. G. & Cowtan, K. (2010). *Acta Cryst.* D**66**, 486–501.
Engh, R. A. & Huber, R. (1991). *Acta Cryst.* A**47**, 392–400.
Grant, A. W., Steel, G., Waugh, H. & Ellis, E. M. (2003). *FEMS Microbiol. Lett.* **218**, 93–99.
Grimshaw, C. E. (1992). *Biochemistry*, **31**, 10139–10145.
Lovell, S. C., Davis, I. W., Arendall, W. B., de Bakker, P. I., Word, J. M., Prisant, M. G., Richardson, J. S. & Richardson, D. C. (2003). *Proteins*, **50**, 437–450.
Matthews, B. W. (1968). *J. Mol. Biol.* **33**, 491–497.
Painter, J. & Merritt, E. A. (2006). *Acta Cryst.* D**62**, 439–450.
Penning, T. M. & Drury, J. E. (2007). *Arch. Biochem. Biophys.* **464**, 241–250.
Rozwarski, D. A., Grant, G. A., Barton, D. H. R., Jacobs, W. R. Jr & Sacchettini, J. C. (1998). *Science*, **279**, 98–102.
Sassetti, C. M., Boyd, D. H. & Rubin, E. J. (2003). *Mol. Microbiol.* **48**, 77–84.
Scoble, J., McAlister, A. D., Fulton, Z., Troy, S., Byres, E., Vivian, J. P., Brammananth, R., Wilce, M. C. J., Le Nours, J., Zaker-Tabrizi, L., Coppel, R. L., Crellin, P. K., Rossjohn, J. & Beddoe, T. (2010). *J. Mol. Biol.* **398**, 26–39.
Timmins, G. S. & Deretic, V. (2006). *Mol. Microbiol.* **62**, 1220–1227.
Winn, M. D. *et al.* (2011). *Acta Cryst.* D**67**, 235–242.
World Health Organization (2013). *Global Tuberculosis Report 2013*. Geneva: World Health Organization. http://www.who.int/tb/publications/global_report/en/.
Zhu, H. (2011). *DSSP and Stride Plugin for PyMOL*. Biotechnology Center (BIOTEC), TU Dresden, Germany. http://www.biotec.tu-dresden.de/~hongboz/dssp_pymol/dssp_pymol.html.